The Effects of Laser Forming on NiTi Superelastic Shape Memory Alloys

Andrew J. Birnbaum

Y. Lawrence Yao

Department of Mechanical Engineering,
Columbia University,
New York, NY 10027

This work focuses on application of the laser forming process to NiTi shape memory alloys. While all NiTi shape memory alloys exhibit both superelasticity and the shape memory effect, this study is restricted to a temperature range over which only the superelastic effect will be active. Specifically, this work addresses laser forming induced macroscopic bending deformations, postprocess residual stress distributions, and changes in microstructure. Like traditional ferrous alloys, the laser forming process may be used as a means for imparting desired permanent deformations in superelastic NiTi alloys. However, this process, when applied to a shape memory alloy also has great potential as a means for shape setting "memorized" geometric configurations while preserving optimal shape memory behavior. Laser forming may be used as a monolithic process, which imparts desired deformation while maintaining desired material behavior. Characterization of the residual stress field, plastic deformation, and phase transformation is carried out numerically and is then subsequently validated via experimental results.
[DOI: 10.1115/1.4000309]

1 Introduction

Shape memory materials due to their highly specialized thermomechanical behavior have received much attention in recent years. These behaviors include the traditional one way shape memory effect (SME), the superelastic effect, and the two-way shape memory effect (TWSME). The mechanism for all three behaviors is rooted in the phase transformation properties of the alloy. The phase transformation may be induced via the application of an external load and/or a change in the alloy temperature.

Laser forming (LF) is a nontraditional manufacturing process whose effects have been extensively characterized at various size scales for an array of materials and alloy systems. The mechanism for deformation is the generation of a transient nonuniform temperature distribution driving local thermal expansion and resulting in controllable permanent deformations. Although some work have been conducted on several classes of materials, the vast majority of investigations are restricted to process application for ferrous alloys [1–3].

NiTi shape memory alloys are typically produced by either vacuum induction melting (VIM) or vacuum arc remelting (VAR) in order to get a homogeneous nickel-titanium alloy constitution. The solidified ingots are then usually hot-worked when large material reductions are required and then cold-worked and annealed in order to get the final product shape, surface finish, refined microstructure, and mechanical properties [4,5]. For most applications, however, shape memory parameters, e.g., phase transformation temperature, recoverable stress, and strain are not acceptable at this stage. An extra mechanical/heat treat step known as "shape setting" are required to optimize these parameters with respect to the desired "memorized" shape. Shape setting of shape memory alloys typically consists of constraining the cold-worked semifinished part in a desired configuration while subjecting it to an appropriate heat treatment in order to achieve the desired part geometry, superelastic, and/or shape memory behavior. This method is limited in that the initial ingot geometry, as well as the final desired geometry, must be fairly simple and requires the design and construction of part-specific fixturing.

The laser forming process avoids these limitations as it relies on thermal rather than direct mechanical means for deformation. It also eliminates the need for hard tooling such as dies and fixtures. Furthermore, due to the inherent local and flexible nature of the process, it may be applied to simple as well as relatively complex initial geometries, as outlined by Cheng and Yao [6].

Besides the ability to form parts with desired final geometries, the laser forming process has recently been shown to have potential as a means for training the two-way shape memory effect [7]. The two-way shape memory effect is characterized by a material's ability to "remember" two distinct configurations. Von Busse et al. showed that through multiple pulsed laser forming of NiTi thin foils, one could "train" the formed part to have two distinct configurations that may be activated solely by thermal means. Laser processing of NiTi shape memory alloys (SMAs) have also recently received attention as a means for thin film deposition [8], laser induced actuation [9], laser annealing [10], and laser machining of NiTi SMA components [11].

2 Process Considerations

While all NiTi shape memory alloys exhibit both superelastic and shape memory effects, this study is restricted to a temperature range over which only the former will be active. Specifically, this work addresses laser induced macroscopic bending deformations, postprocess residual stress distributions, and microstructural and consequences for the phase transformation.

The two prevalent phases exhibited in NiTi shape memory alloys are the "high" temperature BCC Austenitic or parent phase, and the "low" temperature martensitic phase with lower symmetry B19' monoclinic crystal structure. The thermally induced phase transformation is initiated by heating or cooling the material to above or below the respective phase transformation temperatures. The temperatures at which the alloy will be fully austenitic or martensitic are A_f and M_f, respectively. The stress induced phase transformation occurs over temperatures exceeding the austenitic finish temperature accompanied by the application of a load such that the critical stress required for transformation is achieved resulting in the formation of a stress induced martensite (SIM). This is typically performed at temperatures greater than A_f; therefore,

Contributed by the Manufacturing Engineering Division of ASME for publication in the JOURNAL OF MANUFACTURING SCIENCE AND ENGINEERING. Manuscript received November 10, 2006; final manuscript received December 15, 2008; published online July 21, 2010. Assoc. Editor: Kornel F. Ehmann.

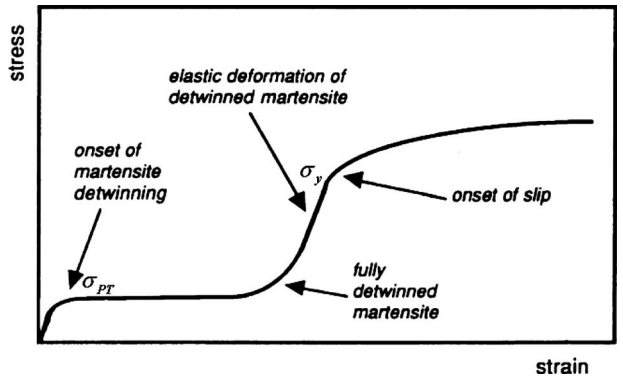

Fig. 1 Characteristic constitutive response of NiTi superelastic shape memory alloy in $A_f < T_{operating} < M_d$ [15]

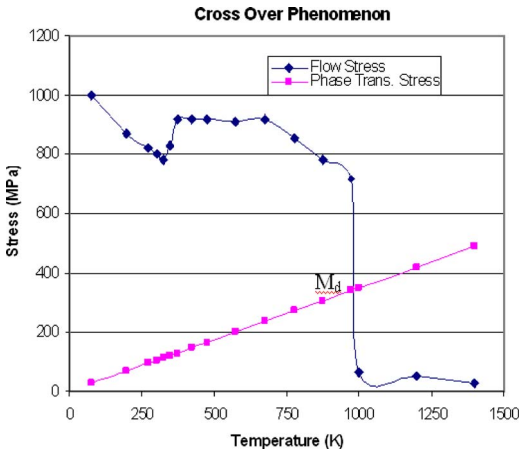

Fig. 2 Temperature dependence of flow stress and critical stress required for phase transformation. Note the cross-over phenomenon occurring just below 1000 K, where the flow stress becomes lower than the stress required for phase transformation. Flow stress at room temperature was obtained from the tensile test performed (Fig. 6). Flow stress variation with temperature, as well as phase transformation stress, was obtained from literature [15].

the initial composition of the alloy is completely austenite. Upon releasing the load, the reverse transformation occurs resulting in complete elastic recovery. Elastic strains of up to 8–9% have been reported [12]. The so-called R-phase characterized by a rhombohedral microstructure also coexists as a transitional phase during the austenite to martensite transformation [13].

The stress/strain response of an austenitic superelastic NiTi alloy is shown in Fig. 1 [14]. It is seen that upon loading there exists a linear elastic regime with an austenitic Young's modulus followed by a nonlinear portion whose start point at σ_{PT} represents the onset of stress induced phase transformation. The range over which this plateau spans is referred to as the transformation strain. Following this plateau, the sample is fully transformed into stress induced martensite. There then exists another linear elastic range that proceeds with the martensitic Young's modulus followed by another nonlinear portion representing the yield curve describing permanent slip and, finally, its ultimate tensile strength. σ_{PT} can be determined via the Clausius–Clapeyron relationship

$$\frac{d\sigma_{PT}}{dT_{eq}} = -\frac{\Delta H}{T_{eq}\varepsilon^t} \tag{1}$$

and is a positive function of temperature, where ε^t, H, and T_{eq} are the transformation strain, enthalpy, and equilibrium phase transformation temperature, respectively. The flow stress, σ_y, of the alloy decreases with increases in temperature. These temperature dependencies become extremely relevant when describing a highly nonuniform thermomechanical process. In fact, at sufficiently high temperatures, there is a temperature, M_d, at which the stress to induce phase transformation is higher than that required for plastic deformation. At this point, the stress induced phase transformation is no longer possible, and the constitutive response of the alloy takes on the more traditional ferrous alloy appearance with an elastic-plastic response. Figure 2 is a plot revealing the crossover temperature for the alloy used in the presented experiments. The temperature dependence of the flow stress, as well as the phase transformation stress, is obtained from literature [15]. This crossover phenomenon adds a considerable amount of complexity to the process analysis, and the implications with respect to the laser forming process are discussed in the numerical approach section.

3 Experimental Conditions and Setup

Experiments were conducted with a CO_2 laser with a maximum 1500 W power output, with a Gaussian intensity distribution. The laser system remained stationary while a precision XY stage translated the specimens along the desired straight path and velocity (Fig. 3). The temperature gradient mechanism (TGM), which is characterized by a steep temperature gradient (TG) through the thickness of the part, is the dominant mechanism for deformation for all presented work. See Ref. [23] for a detailed description of the TGM.

All specimens are rectangular $25 \times 50 \times 0.61$ mm^3 (width by length by thickness), plate of polycrystalline NiTi (Ni-55.82 Ti-balance (wt %)), $A_f = 5\,^\circ$C (by DSC). Samples surfaces were cleaned with methanol then coated with graphite to enhance laser power absorption. Figure 4 shows the as received microstructure through the plate cross section revealing an equiaxed grain structure. In order to observe the microstructural features, all speci-

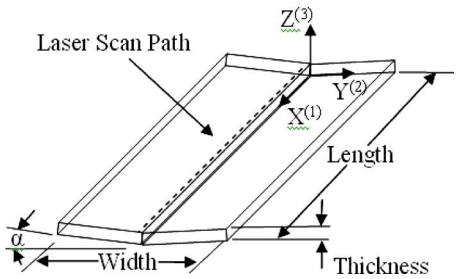

Fig. 3 Schematic of laser-specimen experimental setup

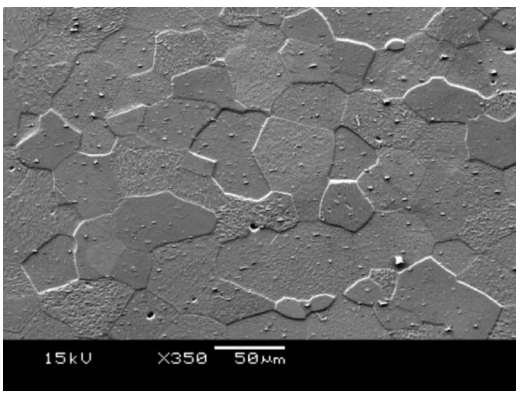

Fig. 4 As received, austenitic grain structure and average grain size ~50 μm. Note the smooth equiaxed grain structure.

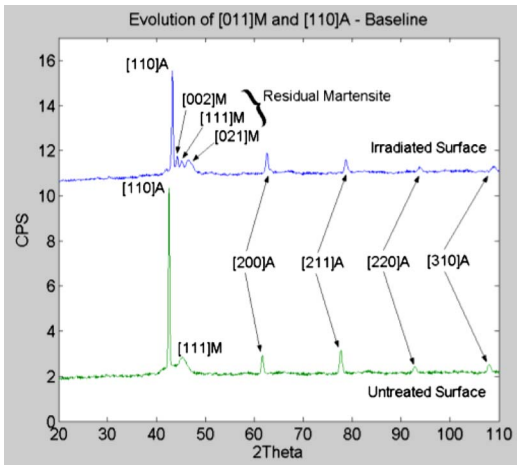

Fig. 5 As received, austenitic X-ray diffraction spectrum at room temperature (A—austenite and M—martensite)

mens were mechanically polished and then etched in a DI water:HNO_3:HF, 5:2:1 solution. Figure 5 shows the as received intensity versus diffraction angle spectrum for the irradiated and untreated portion of the specimen provided by an Inel multiple detector X-ray diffractometer. These figures reveal that despite the heat treatment and annealing it has undergone, as well as its equiaxed grain structure, there is still some preferred texture of the {110} planes presumably due to the rolling of the material as may sometimes be expected [16]. Also shown is that there does exist some residual martensite despite the heat treatment.

All specimens are subjected to an applied power of 250 W at a beam spot diameter of 7 mm, at a velocity of 15 mm/s along a straight scanning path parallel to the edge length. Specimens were subjected to a maximum of five laser scans, with ample time given between scans for cooling so as to ensure thermal effects from previous scans would not affect subsequent ones. The scanning direction remained constant, and specimens were cleaned and received a new coating of graphite between each successive scan so as to maintain consistent optical absorption. Subsequent sectioning of the specimens for observation were accomplished by an electric discharge machine (EDM) so as to minimize the introduction of any further stress due to cutting.

4 Numerical Approach

At the current time, numerical implementation of the constitutive response of superelastic shape memory alloys, as well as the enhancement of the constitutive models themselves, is still under development. DiGiorgi and Saleem [17] provided an extensive review of the constitutive models developed by Tanaka et al. [18], Liang and Rogers [19], and Boyd and Lagoudas [20]. Qidwai's formulation is based on a Gibb's free energy approach

$$G(\sigma,T,\xi,\varepsilon^t) = -\frac{1}{2}\frac{1}{\rho}\sigma{:}S{:}\sigma - \frac{1}{\rho}\sigma{:}[\alpha(T-T_0)+\varepsilon^t] + c\left[(T-T_0) - T\ln\left(\frac{T}{T_0}\right)\right] - \cdots s_0 T + u_0 + f(\xi) \quad (2)$$

has been adopted for use in this work, since it is the most physics based model of the three. σ, ε^t, ξ, T, and T_0 are the Cauchy stress tensor, transformation strain martensitic volume fraction, current temperature, and reference temperature, respectively. S, α, ρ, c, s_0, and u_0 are the effective compliance tensor, effective thermal expansion tensor density, effective specific heat, effective entropy at reference state, and effective internal energy at reference state. The preceding material properties are also calculated via a linear mixture rule

$$S = S^A + \xi(S^M - S^A), \quad \alpha = \alpha^A + \xi(\alpha^M - \alpha^A), \quad c = c^A + \xi(c^M - c^A)$$

$$s_0 = {s_0}^A + \xi({s_0}^M - {s_0}^A), \quad u_0 = {u_0}^A + \xi({u_0}^M - {u_0}^A) \quad (3)$$

where A and M represent austenitic and martensitic properties. The first two terms in Eq. (2) represent contributions to the energy state from elastic strain energy and the strain energy due to thermal expansion phase transformation. The third term represents the change in internal energy due to temperature change. $f(\xi)$ is a hardening function representing the hardening behavior due to phase transformation. A full explanation of the numerical implementation of this constitutive model is available in Qidwai and Lagoudas [21]. ABAQUS has also recently released a subroutine that is capable of simulating the superelastic effect and is phenomenological in nature as opposed to a physics based formulation [22].

Although both of the above mentioned implementations are capable of simulating the superelastic effect, neither combines the superelastic effect with the presence of plastic deformation. This limitation also leads to the inability of simulating the added complexity due to the cross-over phenomenon mentioned in Sec. 3. Just to note, ABAQUS has also recently developed a model that does incorporate the presence of plastic deformation but can only simulate responses below the crossover temperature.

As an approximation, in order to facilitate the simulation of both the plastic and superelastic response, the two phenomena are decoupled into an elastic-plastic simulation, which predicts plastic deformation, followed by a superelastic simulation predicting the local stress induced phase transformation. The former is implemented in the same manner as that of traditional LF modeling techniques [23], i.e., decoupling the thermal from the mechanical process and using the thermal results and transient nonuniform temperature distributions, as input to the mechanical model. The justification for this technique is addressed in Sec. 5.

For the thermal model, boundary conditions are as follows: convection is specified on all plate surfaces, while a moving circular heat source with a Gaussian power distribution specified by a user-defined FORTRAN script simulates the effect of the laser. The temperature dependence of thermal conductivity and specific heat, obtained from both the material supplier and an extensive review of the available literature [15], is also taken into account.

The mechanical models take into account the nonlinear geometric effects stemming from the large deformation theory. The temperature dependence of material properties including Young's modulus, coefficient of thermal expansion, and flow stress are taken into account as well. The temperature dependent mechanical properties used have been obtained existing literature [15]. The values for utilized for the austenitic and martensitic Young's modulus were $E_{\text{aust}}=70$ GPa and $E_{\text{mart}}=30$ GPa. The room temperature flow stress is $\sigma_y=800$ MPa, and the critical stresses for the stress induced phase transformation upon loading and unloading were $\sigma_U^{\text{SIM}}=30$ MPa and $\sigma_L^{\text{SIM}}=350$ MPa.

Numerical models contain 8100 20-node quadratic elements. Attention is given to specifying a fine mesh resolution at and near the scanning path, while away from the scanning path there is a fairly coarse mesh density. Also, as this model is symmetric about the XZ plane, only half of the geometry is modeled to reduce computation time with the appropriate symmetry boundary conditions.

After simulating the thermal field, the resulting temperature distributions are used as inputs to the elastic-plastic mechanical simulation. The elastic-plastic model is then simulated up to time, t_d, corresponding to when the temperature has decreased sufficiently such that the stress required for phase transformation is less than the flow stress of the alloy. At this point the displacement field represents deformations due to elastic and plastic deformations only. The resulting displacement field of the entire model, therefore, the strain field, is then used as input to the superelastic analysis. The strain field is applied by linearly ramping the dis-

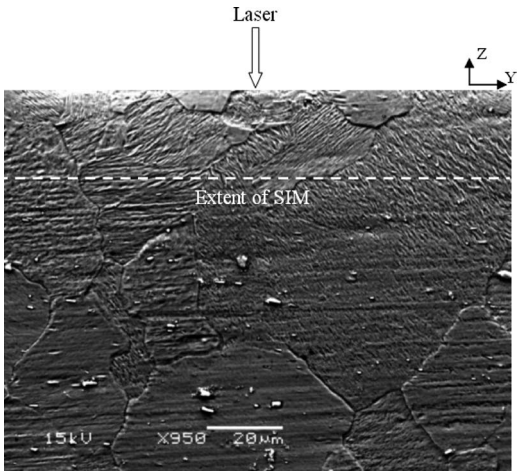

Fig. 6 Micrograph of through thickness cross section of five scan specimen (medium magnification and top surface). Note the transition to SIM as the top surface is approached (*P* =250 W, *v*=15 mm/s, and *d*=7 mm).

placement at each node over 10 s to maintain a quasistatic loading configuration. The superelastic analysis is also simulated isothermally at room temperature. This method was chosen due to the recognition that the residual stress and strain fields are due solely to the presence of the locally plastified region in the heat affected zone.

5 Results and Discussion

5.1 Experimental Characterization. Figure 6 is a micrograph obtained via electron microscopy of the plate cross section perpendicular to the laser scanning direction after five laser scans. As opposed to previous work performed by Fan et al. [24] on the effects of laser forming of Ti64, a distinctive heat affected zone is not readily visible. However, closer inspection of the microstructure near the irradiated and untreated surfaces of the specimen reveal features characteristic of stress induced phase transformation. Figure 7 shows a higher magnified view of the specimen at the irradiated surface near the application of the laser. Martensitic structures can be identified through approximately 40–60 μm

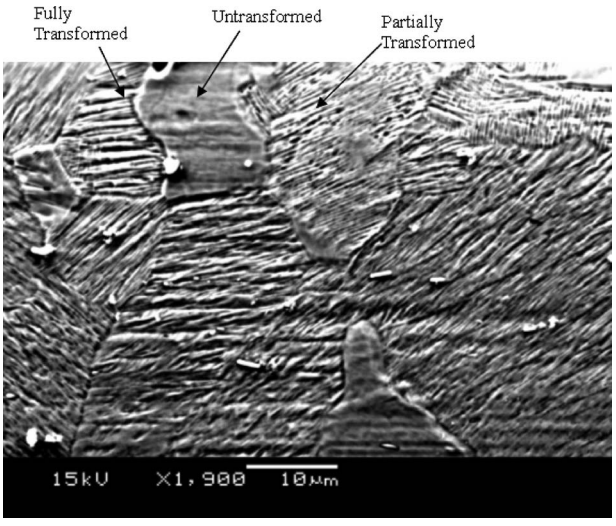

Fig. 7 Micrograph of through thickness cross section of five scan specimen (high magnification and top surface). Note the presence of grains of varying extent of transformation (*P* =250 W, *v*=15 mm/s, and *d*=7 mm).

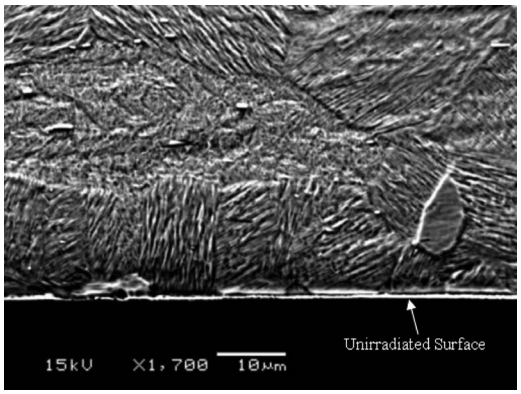

Fig. 8 Micrograph of through thickness cross section of five scan specimen, *P*=250 W, *v*=15 mm/s, and *d*=7 mm (high magnification and bottom surface). Note the presence of SIM.

depth from the specimen's irradiated surface. It also reveals that the extent of phase transformation varies among grains. Several grains are identified as being fully, partially, or not transformed at all. Brinson et al. [25] reported similar findings in in situ uniaxial tensile tests concluding that grains must be favorably oriented with respect to the application of stress in order to undergo the stress induced phase transformation. Therefore grains of various degrees of transformation may coexist. Also, it is important to note that although laser forming imparts significant thermal energy, the specimen is austenitic at room temperature, and therefore all phase transformation that occurs must be stress induced as the part is only subjected to increases in temperature and subsequently cools back to room temperature. Figure 8 shows the cross section at the same *Y* location but at the untreated of the specimen surface. Although SIM are identifiable, a sharp boundary revealing a well defined extent/depth is not.

Figures 9 and 10 are X-ray diffraction (XRD) spectrums taken at representative locations along the laser scan path at the irradiated and untreated surfaces for multiple scans revealing an increase in martensite at the expense of the existing austenitic content as the number of scans increases. This may be expected as

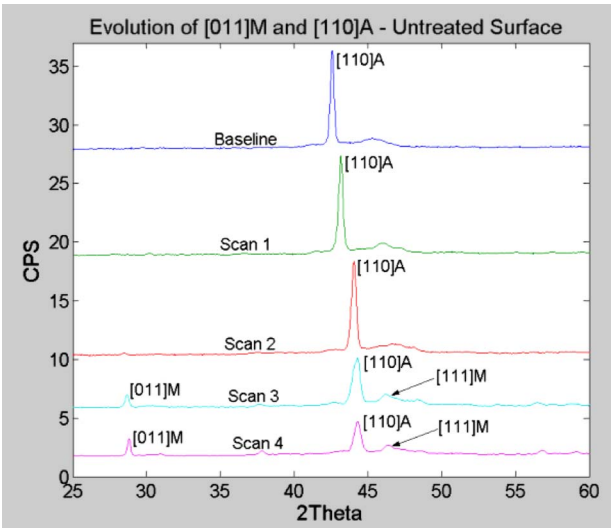

Fig. 9 X-ray diffraction spectra over successive scans (*P* =250 W, *v*=15 mm/s, and *d*=7 mm) revealing an increase in martensitic content at the expense of the parent austenitic matrix (untreated surface). The [110] positive peak shift is due to tensile residual stress (*Y*-direction) induced by the LF process. (A—austenite and M—martensite).

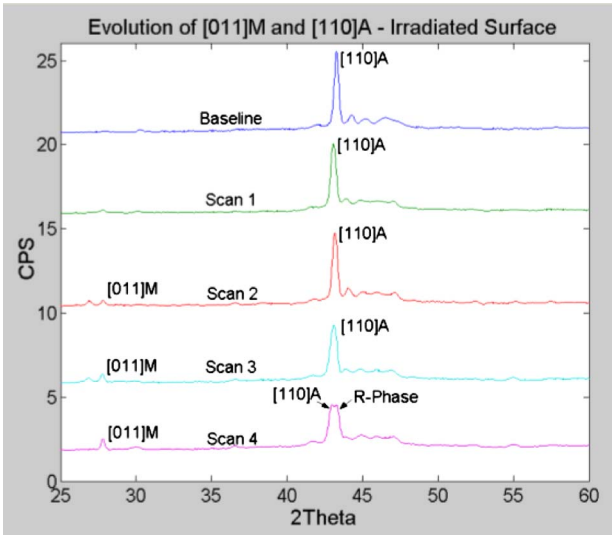

Fig. 10 X-ray diffraction spectra over successive scans (*P*=250 W, *v*=15 mm/s, and *d*=7 mm) revealing an increase in martensitic content at the expense of the parent austenitic matrix (irradiated surface). Note the presence of R-phase in the fourth scan (A—austenite and M—martensite). Also note the negative peak shift from the baseline corresponding to compressive residual stress (*Y*-direction) in the irradiated surface.

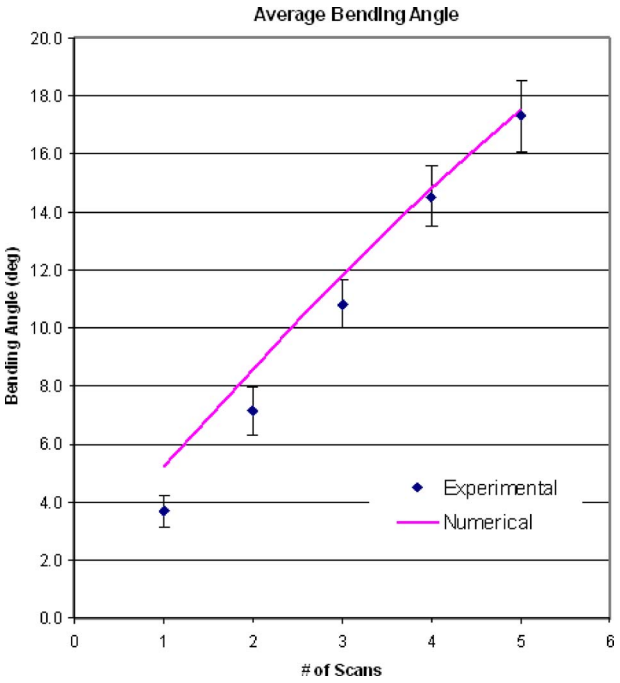

Fig. 11 Numerical and experimental average bending angle, *P*=250 W, *v*=15 mm/s, and *d*=7 mm

plastic strain increases with each scan increasing the spatial extent of residual stresses whose magnitudes are sufficiently large to induce phase transformation. The formation of the transitional R-phase may also be seen upon the fourth laser scan on the irradiated surface. Currently it is undetermined as to what the relative contributions are to the observed increase in martensitic volume fraction; whether it is due to a further transformation of already transforming grains or increases in residual stress further from the laser scan path leading to the initiation of new grains transforming. This is due to the fact that the volume of material irradiated by the X-rays is on the order of the laser spot size. Figure 9 also reveals a distinctive peak shift in the positive 2θ direction indicating a decreasing lattice constant in the *Z*-direction and thus a tensile residual stress in the *Y*-direction on the untreated surface. Similarly, a slight peak shift in the negative 2θ direction is seen in Fig. 10, indicating a state of compressive residual stress on the irradiated surface. It is interesting to note that the peak shifts are dramatic for the first two scans and are not as extreme for subsequent scans in the untreated surface. This would suggest that plastic deformation in the untreated surface is not significant until the second scan, whereas the irradiated surface is plastified upon the first. These "steady state" peak locations are consistent with lattice constants due to strains corresponding states of stress equal to the room temperature flow stress of the material.

5.2 Numerical Results and Validation. Figure 11 shows a plot of both the numerically predicted and experimentally observed average bending angles. This average is based upon measurements taken at five locations along the laser scan path. It is seen that the error between the measured and predicted values decreases significantly as the number of scans is increased resulting in predictions to within 2% of the experiment for the five scan case. The source of the errors and the decrease in error for subsequent scans is discussed below.

Figures 12 shows experimental and numerical results for the bending angle distribution along the laser scan path (*x*-direction). A monotonic decrease in relative error is also seen as the number of scans is increased. This is somewhat counterintuitive, as one may expect, that with each successive scan there is an increase in the volume fraction of martensite, and thus the local properties would continue to change resulting in an increasing error. However, even with the introduction of further martensite, the application of the laser in successive scans results in a thermally induced martensite to austenite transformation as further plastic deformation occurs resulting in a fully austenitic condition for each scan.

Although the numerically predicted average bending angle compares quite well with the experimentally observed (Fig. 11), there is significant error in predicting the bending angle distribution along the laser scan direction. The main source or error stems

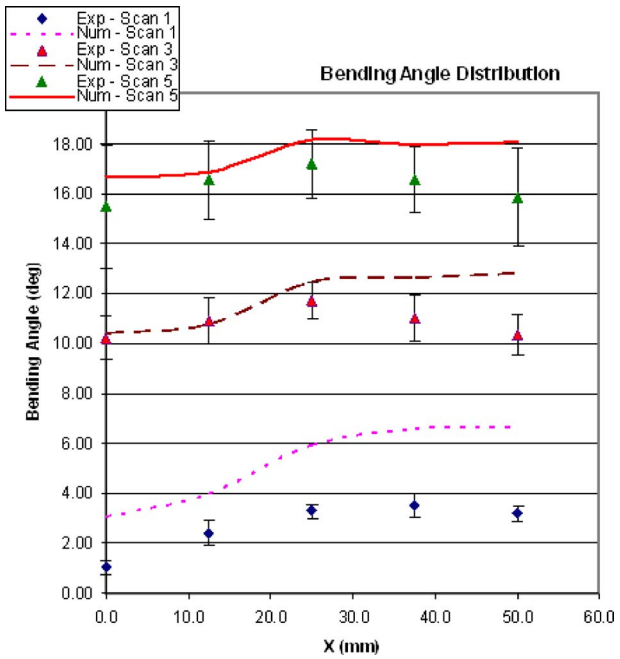

Fig. 12 Bending angle distribution along laser scan path for varying numbers of laser scans. *P*=250 W, *v*=15 mm/s, and *d*=7 mm.

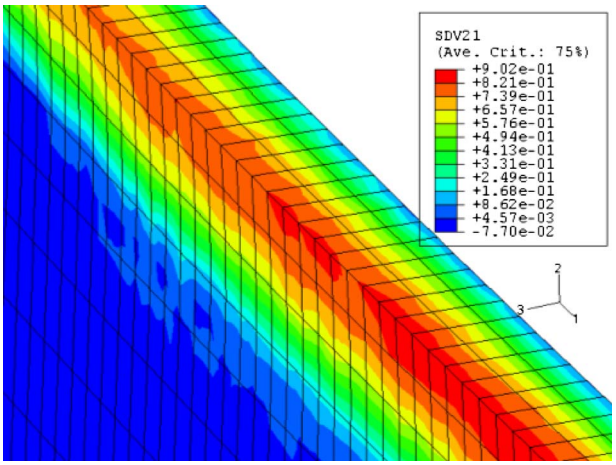

Fig. 13 Contour plot of martensitic volume fraction (*P*=250 W, *v*=15 mm/s, and *d*=7 mm)

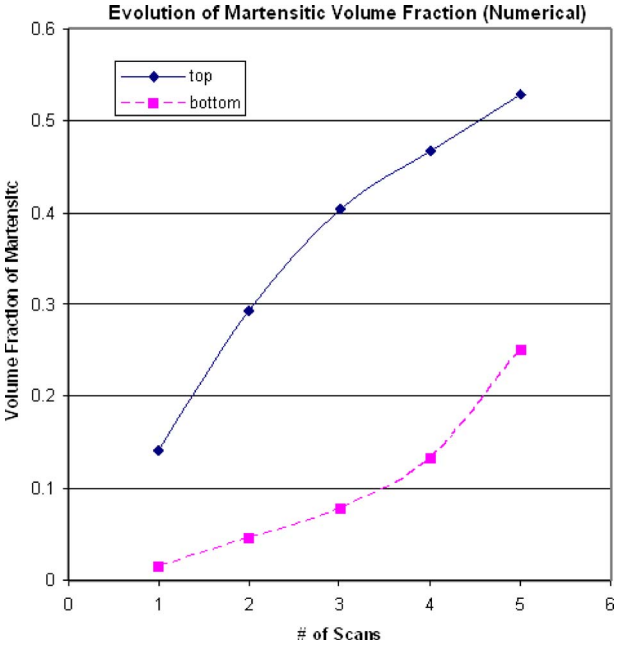

Fig. 14 Numerically predicted changes in martensitic volume fraction as a function of the number of laser scans for the top and bottom surfaces (*P*=250 W, *v*=15 mm/s, and *d*=7 mm)

from difficulties in predicting deformation, when strains due to phase transformation are on the same order as strains due to plastic deformation. An additional source of error is a lack of temperature dependent material data, particularly, at significantly elevated temperatures. The other significant contributor to error relates to effects stemming from the presence of free edges [26]. These effects are magnified in this case due to the fact that near the free edges, the plastic strains in the *Y* direction decrease and, again, the magnitudes of the phase transformation strains become comparable, thus, increasing the error. This is seen near the free edges for the three and five scan cases in Fig. 12.

As discussed in the numerical approach, the traditional laser forming model is capable of accurately predicting the extent of plastic deformation, but fails to predict the postprocess superelastic response of the material. This suggests that the transformation strains upon cooling down are on the same order of magnitude of the plastic strains for lower numbers of scans, but the plastic to transformation strain ratio must also be increasing with respect to increases in laser scans. Referring to the uniaxial tensile test, the maximum transformation strain, the strain at which full transformation occurs, is on the order of 7.5%. The laser forming simulations reveal that plastic strains are on the order of 8% by the third scan. At this point, at least a portion of grains in regions of higher strains have fully transformed, as confirmed by micrograph inspection. Although further elastic strains may be produced in the linear martensitic range, micrographs confirm that phase transformation is limited to approximately 20–30 μm and 40–60 μm into the depth for the irradiated untreated surfaces, respectively, while the forming model predicts plastic strains on the order of 8% even 0.3 mm through the depth of the plate. Therefore subsequent scans must result in increases in plastic strain with respect to transformation strains resulting in plastic deformation being the dominant mechanism for macroscopic deformation. This explains the increased model accuracy at higher numbers of scans.

Figure 13 is a contour plot of martensitic volume fraction from the superelastic simulation. It predicts local increases in martensitic volume fraction due to the resulting residual stress field. It also shows a monotonic decrease in volume fraction as distance through the thickness and perpendicular to the laser scan is increased. Figure 14 shows the numerically predicted average martensitic volume fraction. The average was taken across nodes perpendicular to the laser scan path at a distance equal to the extent of the distance irradiated by the X-ray in the respective experiments. It reveals that both the irradiated and untreated surfaces have a monotonically increasing martensitic volume fraction. This is confirmed by the X-ray diffraction results presented in Figs. 9 and 10. However, some discrepancies, particularly, with respect to the micrographs in Figs. 6 and 8 remain. For example, the micrographs clearly show that the martensitic structures are limited to within fairly shallow depths near the irradiated and untreated surfaces, while the numerical model predicts a fair amount of martensite through the entire thickness. This may be explained as follows. Due to the nature of the phase transformation models, the change in martensitic volume fraction closely resembles the von-Mises distributions in both Lagoudas' Gibb's energy formulation and especially the ABAQUS transformation potential approach. Both depend on all components of stress and strain for predicting the resultant volume fraction increment. However, in order to examine the cross section of the specimen, it was sectioned with an EDM. This sectioning results in a new traction free face and must have resulted in the relaxation of the normal stresses in the *X* direction and the shear stresses τ_{12} and τ_{13}. This relaxation was most likely also accompanied by a reverse phase transformation of stress induced martensite back to austenite. This explains the presence of martensitic structures in an area limited to near both surfaces.

5.3 Effects of Variations in Process Parameters. Several further numerical simulations with varying operating parameters have also been conducted. These simulations are performed to examine the effect of the maximum through thickness temperature gradient on the resulting bending deformation and martensitic volume fraction. The temperature gradient is seen as the driving force for bending deformation and is defined as $TG=(T_i-T_u)/s$, where T_i is the temperature of a representative point on the irradiated surface on the scan path, T_u is the temperature of a point with the same *X* and *Y* coordinates but on the untreated surface, and *s* is the sheet thickness. For consistency, the peak processing temperature has been chosen as a guideline for the choice of operating parameters. Thus the combinations of power and velocity listed in Table 1 have been chosen such that the peak process temperatures are all 1550 K.

Figure 15 is a plot of martensitic volume fraction as a function of the distance from the scan path. It is seen that for the minimum temperature gradient there is a full transformation, and the transformed material extends a distance from the scan path, whereas the distributions with higher temperature gradients are fully trans-

Table 1 Process parameters for numerical simulations with resulting through thickness temperature gradients. Note all simulations are run using a 7 mm laser spot diameter and result in the same peak processing temperature.

Case	Power (W)	Velocity (mm/s)	Temperature gradient (K/mm)
1	250	15	308
2	515	35	589
3	725	55	825
4	920	75	1040
5	1075	95	1196

formed near the scan path but quickly drop off as the distance increases. Figure 16 shows plots of the average bending angle and average volume fraction as a function of laser scans on the irradiated surface for two different temperature gradients. This reveals that both can be accurately approximated as linear functions up to five scans. More importantly it shows that while the average bending angles for both temperature gradients increase at roughly the same rate, the volume fraction for the lower temperature gradient increases at a much higher rate as the number of laser scans increases. This provides practical insight into that if the intended use of the laser forming process is to be used as a shape setting method and the martensitic volume fraction should be minimized, it follows that it is advantageous to operate at higher temperature gradients and higher numbers of scans.

As a first approximation, to facilitate the modeling of the laser forming process, the plastification process, and the superelastic response are decoupled. The validity of this approximation is now addressed. Figure 17 shows the temperature and normal plastic strain time history of a representative point on the laser scan path. The laser arrives at that point at $t=2.5$ s. Within 0.16 s of the laser arrival, the temperature of the point has reached the cross-over temperature described in Sec. 4. At this time, less than 0.3% plastic strain maximum has been generated, suggesting that the constitutive response in close proximity to the laser is solely elastic-plastic with no stress induced phase transformation; and so, during forming the constitutive response including plastic deformation is very much like that of traditional ferrous alloys. The stress induced martensite then forms upon the specimen cooling down to temperatures below the cross-over temperature due to the residual stress field created by the presence of local plastic strain.

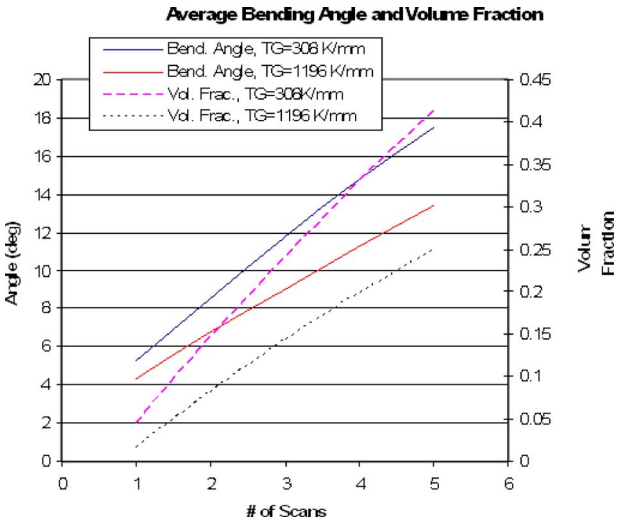

Fig. 16 Average bending angle and martensitic volume fraction as a function of laser scans for selected temperature gradients

6 Conclusion

In conclusion, it has been shown that laser forming of shape memory alloys that are austenitic at ambient temperatures does lead to the formation of stress induced martensite due to the post-process residual stress resulting from local plastic deformation. Furthermore, it has also been shown that traditional techniques for numerically simulating the laser forming process can accurately predict the macroscopic deformation of specimens, especially in multiple scan applications, where plastic deformation is the dominant mechanism for deformation rather than deformation due to phase transformation.

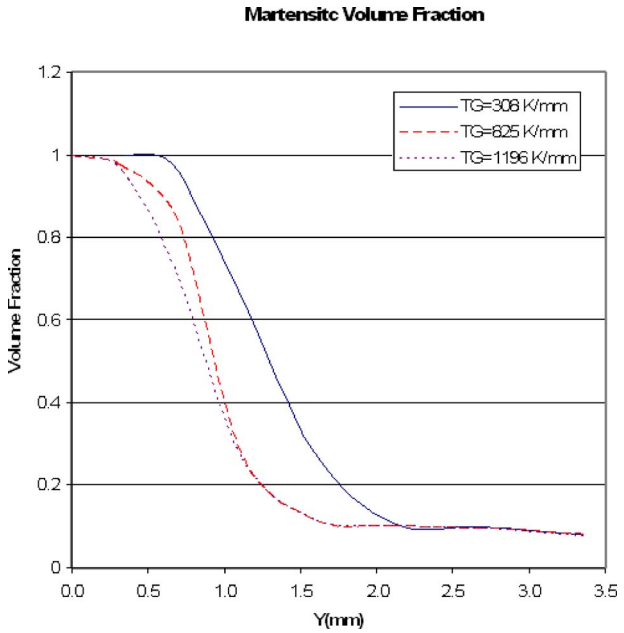

Fig. 15 Martensitic volume fraction distribution perpendicular to laser scan on irradiated surface for three distinct temperature gradients

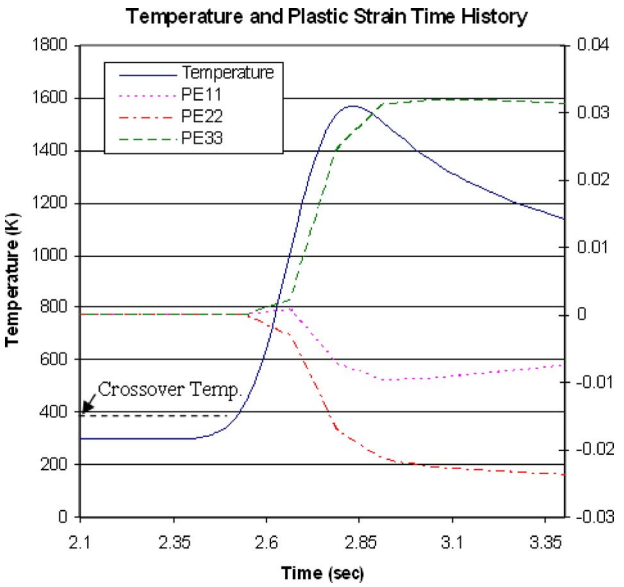

Fig. 17 Temperature and plastic strain time history at a representative point on the laser scan path. Laser arrives at $t=2.5$ s ($P=250$ W, $v=15$ mm/s, and $d=7$ mm).

Traditional shape setting methods require fixture design, a method for constraint, and due to competing factors, there are difficulties in producing complex geometries with optimal shape memory properties concurrently. In the current study, the presence of stress induced martensite has been shown to be local, implying the change in microstructure and macroscopic properties of the overall part remain relatively unaffected. Therefore, the desired shape memory properties may be imparted to the component in a simple initial form such as a plate, tube, foil, etc., and then the laser forming process may be used to induce the final desired deformation, providing a significant improvement over currently utilized shape setting methods. Furthermore, it has been shown that operating at higher temperature gradients, although producing less bending deformation will result in lower martensitic volume fractions and, thus, is advantageous when using the laser forming process as a means for shape setting.

Currently, due to the complexities stemming from the process and material itself, the analysis presented is predominantly qualitative in nature. Obtaining quantitative information pertaining to the actual volume fraction of martensite from X-ray diffraction via integrated intensity ratios is not practical due to the aforementioned preferred {110}, the presence of significant plastic deformation resulting in peak widening and R-phase formation resulting in diffracted peaks near austenitic peaks. However, a future investigation can utilize a spatially resolved characterization method, such as electron back-scatter diffraction (EBSD), to characterize the stress induced phase transformation zone in the plate cross section. Additionally, a future study may also seek to extend the current analysis via XRD peak decompositions (austenite and R-phase) in order to accurately determine the austenitic peak shifts for calculating the residual stress field that develops upon laser processing. Both of these approaches would provide a more quantitative measure of the process induced microstructural modification and residual stress field.

Acknowledgment

This work is supported in part by NSF under Grant No. DMI-0355432 and Columbia University. Special thanks are also extended to Professor Dimitris Lagoudas for the provision of the superelastic user-defined subroutine.

References

[1] Fan, Y., Yang, Z., Cheng, P., Egland, K., and Yao, Y. L., 2005, "Numerical and Experimental Investigation of Microstructure Evolution and Mechanical Behavior of Steel in Laser Forming," ASME J. Manuf. Sci. Eng., accepted.
[2] Li, W., and Yao, Y. L., 2000, "Numerical and Experimental Study of Strain Rate Effects in Laser Forming," ASME J. Manuf. Sci. Eng., **122**(3), pp. 445–451.
[3] Thomson, G., 2001, "Material Property Changes Associated With Laser Forming of Mild Steel Components," J. Mater. Process. Technol., **118**(1–3), pp. 40–44.
[4] Pelton, A., Russell, S. M., and DiCello, J., 2003, "The Physical Metallurgy of Nitinol for Medical Applications," JOM, **55**(5), pp. 33–37.
[5] Otsuka, K., and Wayman, C. M., 1998, *Shape Memory Materials*, Cambridge University Press, Cambridge, England.
[6] Cheng, J., and Yao, Y. L., 2004, "Process Design of Laser Forming for Three Dimensional Thin Plates," ASME J. Manuf. Sci. Eng., **126**(2), pp. 217–225.
[7] Ostendorf, A., Paschko, S., von Busse, A., Bunte, J., Hustedt, M., and Fargas, M., 2004, "Laser-Based Induction of the Two-Way Memory Effect into Shape Memory Alloy Components," Proc. SPIE, **5662**, pp. 586–592.
[8] Chen, X. Y., Lu, Y. F., Ren, Z. M., Zhang, L., Wang, J. P., and Liew, T., 2001, Mater. Res. Soc. Symp. Proc., **672**, pp. O10.12.1–O10.12.6.
[9] Zalalutdinov, M., Aubin, K., Reichenbach, R., Zehnder, A., Houston, B., Parpia, J., and Craighead, H., 2003, "Shell-Type Micromechanical Actuator and Resonator," Appl. Phys. Lett., **83**(18), pp. 3815–3817.
[10] Bellouard, Y., Lehnert, T., Clavel, R., Sidler, T., and Gotthardt, R., 2001, "Laser Annealing of Shape Memory Alloys: A Versatile Tool for Developing Smart Micro-Devices," J. Phys. IV, **11**(8), pp. 8571–8576.
[11] Haferkamp, H., Goede, M., and Leester-Schaedel, M., 1999, "Keeping the Shape Memory Properties of Miniaturized Components of NiTi-Alloys by Laser Machining," Proc. SPIE, **3675**, pp. 267–274.
[12] Nemat-Nasser, S., 2006, "Superelastic and Cyclic Response on NiTi SMA at Various Strain Rates and Temperatures," Mech. Mater., **38**(5–6), pp. 463–474.
[13] Miyazaki, S., Kimura, S., and Otsuka, K., 1988, "Shape-Memory Effect and Pseudoelasticity Associated With the R-Phase Transition in Ti-50 at % Ni Single Crystals," Philos. Mag. A, **57**(3), pp. 467–478.
[14] Turner, T., 2001, "Thermo-Mechanical Response of Shape Memory Alloy Hybrid Composites," Report No. NASA/TM-2001-210656.
[15] Jackson, C. M., Wagner, H. J., and Wasilewski, R. J., 1972, "55-Nitinol—The Alloy With a Memory: Its Physical Metallurgy, Properties and Applications," NASA Publication No. SP5110.
[16] Cullity, B. D., 1959, *Elements of X-Ray Diffraction*, Addison-Wesley, Reading, MA.
[17] DeGiorgi, V. G., and Saleem, H., 1999, "A Review of a Few Shape Memory Alloy Constitutive Models," Proc. SPIE, **3667**, pp. 730–737.
[18] Tanaka, K., Hayashi, T., and Itoh, Y., 1992, "Analysis of Thermo-Mechanical Behavior of Shape Memory Alloys," Mech. Mater., **13**, pp. 207–215.
[19] Liang, C., and Rogers, C. A., 1992, "A Multi-Dimensional Constitutive Model for Shape Memory Alloys," J. Eng. Math., **26**, pp. 429–443.
[20] Boyd, J., and Lagoudas, D. C., 1996, "A Thermodynamic Constitutive Model for Shape Memory Materials. Part I. The Monolithic Shape Memory Alloy," Int. J. Plast., **12**(6), pp. 805–842.
[21] Qidwai, M. A., and Lagoudas, D. C., 2000, "Numerical Implementation of a Shape Memory Alloy Thermo-Mechanical Constitutive Model Using Return Mapping Algorithms," Int. J. Numer. Methods Eng., **47**(6), pp. 1123–1168.
[22] Rebelo, N., Walker, N., and Foadian, H., 2001, "Simulation of Implantable Nitinol Stents," ABAQUS User's Conference, pp. 1–14.
[23] Birnbaum, A. J., Cheng, P., and Yao, Y. L., "Effects of Clamping on Laser Forming Process," ASME J. Manuf. Sci. Eng., accepted.
[24] Fan, Y., Cheng, P., Yao, Y. L., Yang, Z., and Egland, K., 2005, "Effects of Phase Transformations on Laser Forming of Ti-6Al-4V Alloy," J. Appl. Phys., **98**, p. 013518.
[25] Brinson, C., Schmidt, I., and Lammering, R., 2004, "Stress-Induced Transformation Behavior of a Polycrystalline NiTi Shape Memory Alloy: Micro and Macromechanical Investigations Via In Situ Optical Microscopy," J. Mech. Phys. Solids, **52**, pp. 1549–1571.
[26] Bao, J., and Yao, Y. L., 2001, "Analysis and Prediction of Edge Effects in Laser Bending," ASME J. Manuf. Sci. Eng., **123**, pp. 53–61.